Supplementary Information

Synergistic Enhancement of Bilayer NiOOH Catalytic Activity for Oxygen Evolution Reaction via Interface and Fe Doping: Insights from First-Principles Calculations

Xing-Chen Ding, [a] Jia-Hang Cai, [a] Rui Tan, [a] Xing-Xing Jiang, [a] Jie-Yao Tan, [a] Qi-Hu,[b] Zhen-Kun Tang, [a,*] Li-Min Liu[b,*]

AFFILIATIONS

[a] *Key Laboratory of Micro-nano Energy Materials and Application Technologies, University of Hunan Province & College of Physics and Electronics Engineering, Hengyang Normal University, Hengyang 421002, China*

[b] *School of Physics, Beihang University, Beijing 100191, China*

[*] **Author to whom correspondence should be addressed:** zktang@hynu.edu.cn (Z.-K. Tang), liminliu@buaa.edu.cn (L.-M. Liu)

The Oxygen Evolution Reaction (OER) process involves the dissociation and adsorption of various oxygen-containing intermediates, constituting a complex multi-step reaction pathway. Typically, the reaction comprises four fundamental steps under alkaline conditions,[1] which are described as:

$$* + OH^- \rightarrow {}^*OH + e^- \quad \text{(S1)}$$

$${}^*OH + OH^- \rightarrow {}^*O + H_2O + e^- \quad \text{(S2)}$$

$${}^*O + OH^- \rightarrow {}^*OOH + e^- \quad \text{(S3)}$$

$${}^*OOH + OH^- \rightarrow * + O_2(g) + H_2O + e^- \quad \text{(S4)}$$

Where * denotes the surface-active site, (l) and (g) represent liquid and gas phases, respectively. ${}^*OH$, ${}^*O$, and ${}^*OOH$ represent adsorbed intermediates.[2] The Gibbs free energy change ΔG_i (i=1, 2, 3, 4) for the OER step can be defined as:[3]

$$\Delta G_i = \Delta E + \Delta ZPE - T\Delta S \quad \text{(S5)}$$

The term ΔE represents the reaction energy difference between reactants and products. ΔZPE stands for zero-point energy, ΔS is the entropy difference between adsorbed and independent states, and T is the reaction temperature (T= 298.15 K). By calculating the vibrational frequencies of adsorbates on the catalyst, the contribution of ZPE in the free energy expression was determined.[4]

By evaluating the catalytic performance through the potential steps of the OER, the overpotential (η_{OER}) was proposed under ideal conditions of U = 0 and the Standard Hydrogen Electrode (SHE),[5] defined as:

$$\eta_{OER} = \max(\Delta G)/e - 1.23V \quad \text{(S6)}$$

In the equation, η_{OER} represents the overpotential for the oxygen evolution reaction (OER). Generally, a lower η_{OER} indicates higher catalytic activity.

To compare the relative stability of the Fe-doped bilayer NiOOH structures, the formation energies (E_f) for Fe substituting Ni is defined as:

$$E_f = E_{dope} - (E_p - \mu_{Ni} + \mu_{Fe}) \quad \text{(S7)}$$

Where E_p and E_{dope} represent the total energies of the pristine and doped bilayer NiOOH, respectively. μ_{Ni} and μ_{Fe} are the chemical potential of Ni and Fe atoms.

The formation of O vacancies and OH vacancies can be calculated respectively by the following equations:

$$E_f(V_O) = E_{NiFeOOH-V_O} - E_{NiFeOOH} + \mu_O \quad \text{(S8)}$$

$$E_f(V_{OH}) = E_{NiFeOOH-V_{OH}} - E_{NiFeOOH} + \mu_O + \mu_H \quad \text{(S9)}$$

Where $E_{NiFeOOH-V_O}$ and $E_{NiFeOOH-V_{OH}}$ represent the total energy of the

NiFeOOH without O vacancies and OH vacancies, respectively, $E_{NiFeOOH}$ represent the energy of the NiFeOOH, μ_O and μ_H are the chemical potential of O and OH atom respectively.

The valence electron configurations that have been explicitly taken into account are: Ni with $3d^8 4s^2$, Fe with $3d^7 4s^1$, O with $2s^2 2p^4$, and H with $1s^1$.

In the calculations of vacancy formation energies and dopant formation energies, the chemical potential of O was taken as the average formation enthalpy of O_2 under the same lattice framework. Under anion-rich conditions, the chemical potentials of Ni, Fe and H were referenced to their corresponding oxide phases, NiO, Fe_2O_3 and H_2O, respectively. In particular, μ_{Ni}, μ_{Fe} and μ_H were determined from the total energies of NiO, Fe_2O_3 and H_2O, and then the energy contribution of oxygen was subtracted according to the adopted μ_O, as described by the following equations:

$$\mu_{Ni} = E(NiO) - \mu_O \tag{S10}$$

$$\mu_{Fe} = \frac{E(Fe_2O_3) - 3\mu_O}{2} \tag{S11}$$

$$\mu_H = \frac{E(H_2O) - \mu_O}{2} \tag{S12}$$

The outcomes of the cutoff energy test reveal that as the cutoff energy value increases incrementally, the total energy of the $Ni_{75\%}Fe_{25\%}OOH$ system gradually demonstrates a converging pattern once it surpasses 450 eV. It is noteworthy that the recommended cutoff energy for the PAW pseudopotential of oxygen (O) atoms is generally higher than 400 eV. Therefore, the computational results with a cutoff energy below 400 eV are unreliable. Similar findings emerge from the tests carried out on bulk nickel hydroxide ($Ni(OH)_2$) and nickel oxyhydroxide (NiOOH), as elaborated in Figure S13. Taking into account all the aforementioned test results, it is entirely justifiable for this study to opt for 500 eV as the plane-wave cutoff energy. Moreover, we conducted tests on six distinct k-point grids, specifically 1×1×1, 2×1×1, 4×2×1, 6×3×1, 8×4×1, and 10×5×1. Our findings indicate that the 6×3×1 k-point grid is also adequate to guarantee the reliability of the structural optimization results, while simultaneously achieving a reasonable equilibrium between computational accuracy and cost.

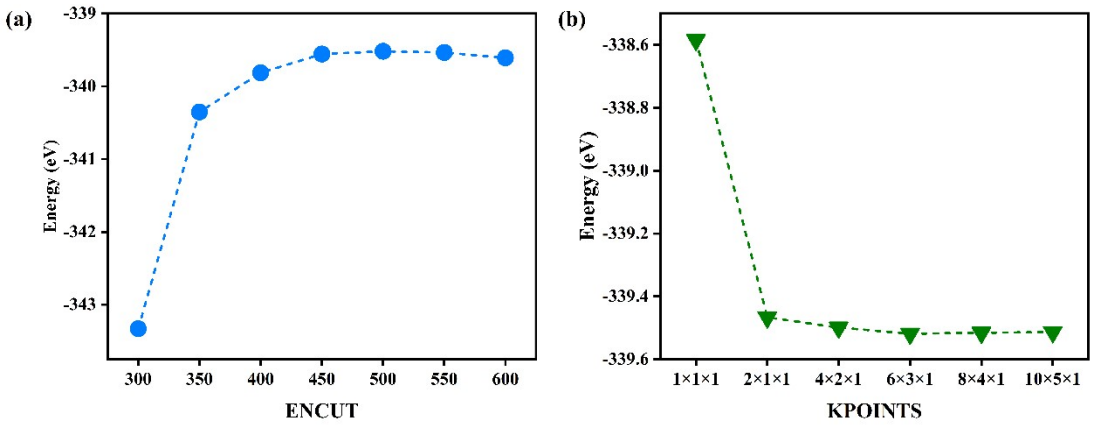

Fig. S1 (a-b) Energy convergence test of the plane-wave cutoff energy and k-point mesh for $Ni_{75\%}Fe_{25\%}OOH$ (Fe A-C).

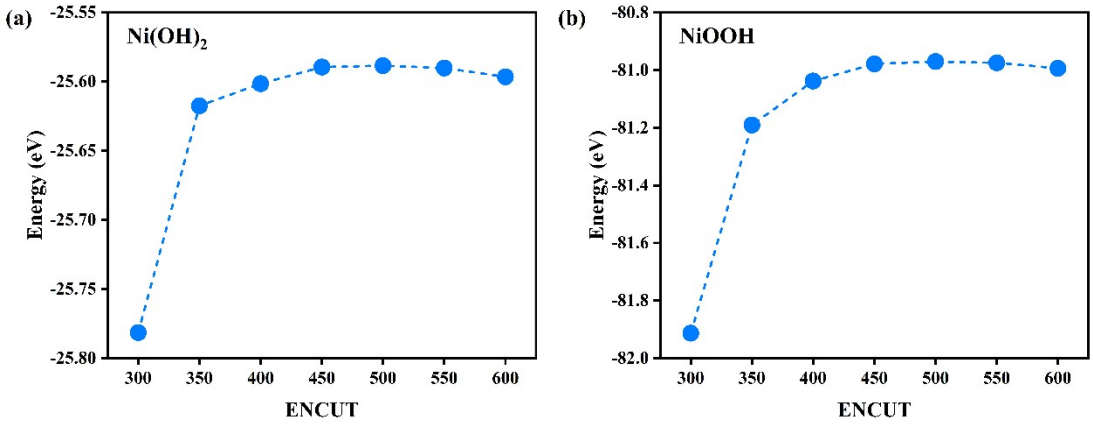

Fig. S2 (a-b) Energy convergence test of the plane-wave cutoff energy for (a) $Ni(OH)_2$ and (b) NiOOH systems.

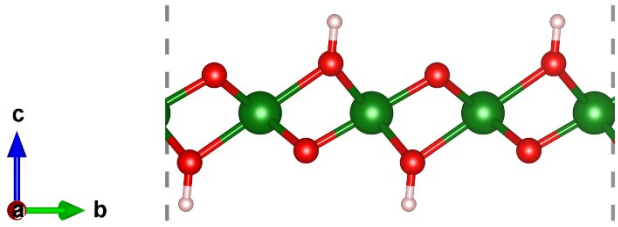

Fig. S3 The geometric structure of monolayer NiOOH. Green, red, and pink spheres represent Ni, O, and H atoms, respectively.

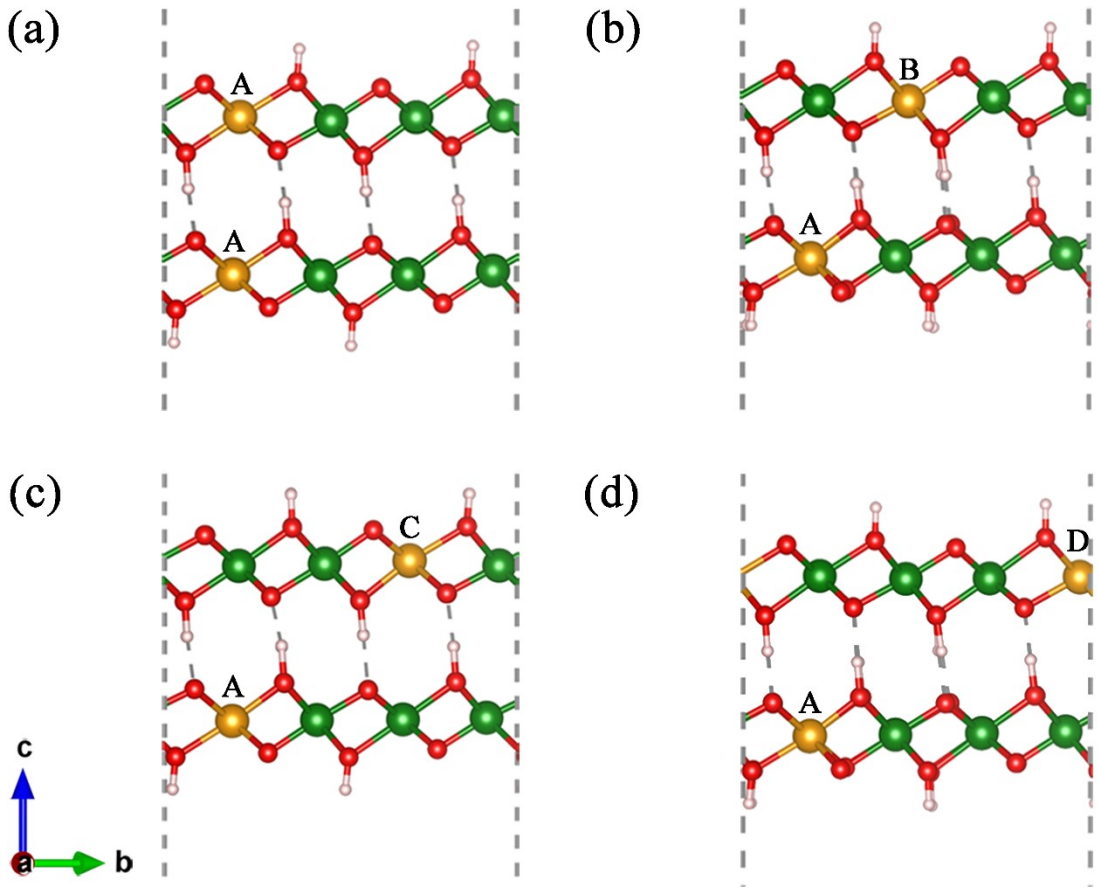

Fig. S4 The geometric structures of (a) $Ni_{75\%}Fe_{25\%}OOH$ (Fe A-A); (b) $Ni_{75\%}Fe_{25\%}OOH$ (Fe A-B); (c) $Ni_{75\%}Fe_{25\%}OOH$ (Fe A-C); (d) $Ni_{75\%}Fe_{25\%}OOH$ (Fe A-D). Yellow, green, red, and pink spheres represent Ni, Fe, O, and H atoms, respectively.

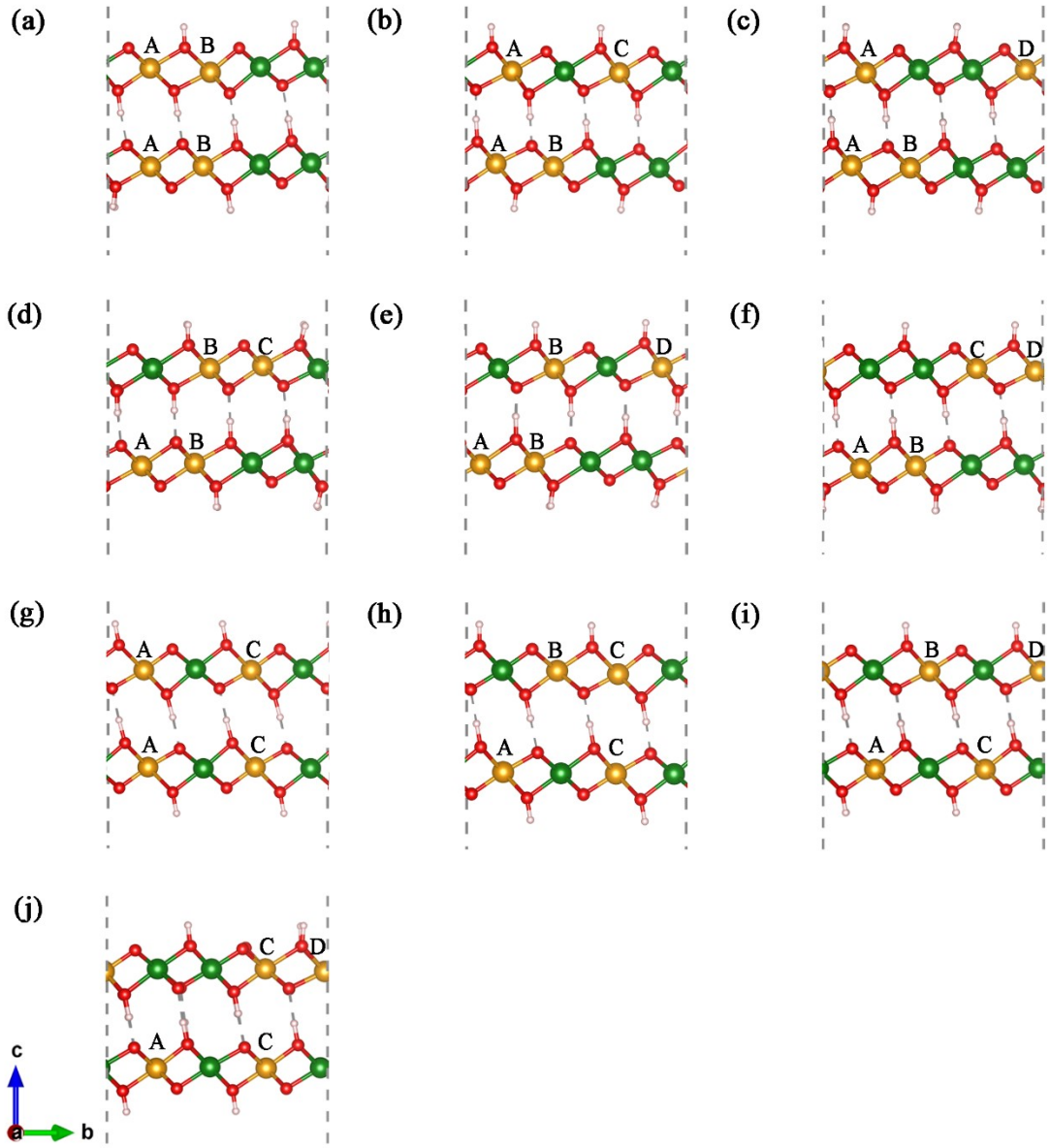

Fig. S5 The geometric structures of (a) $Ni_{50\%}Fe_{50\%}OOH$ (Fe AB-AB); (b) $Ni_{50\%}Fe_{50\%}OOH$ (Fe AB-AC); (c) $Ni_{50\%}Fe_{50\%}OOH$ (Fe AB-AD); (d) $Ni_{50\%}Fe_{50\%}OOH$ (Fe AB-BC); (e) $Ni_{50\%}Fe_{50\%}OOH$ (Fe AB-BD); (f) $Ni_{50\%}Fe_{50\%}OOH$ (Fe AB-CD); (g) $Ni_{50\%}Fe_{50\%}OOH$ (Fe AC-AC); (h) $Ni_{50\%}Fe_{50\%}OOH$ (Fe AC-BC); (i) $Ni_{50\%}Fe_{50\%}OOH$ (Fe AC-BD); (j) $Ni_{50\%}Fe_{50\%}OOH$ (Fe AC-CD). Yellow, green, red, and pink spheres represent Ni, Fe, O, and H atoms, respectively.

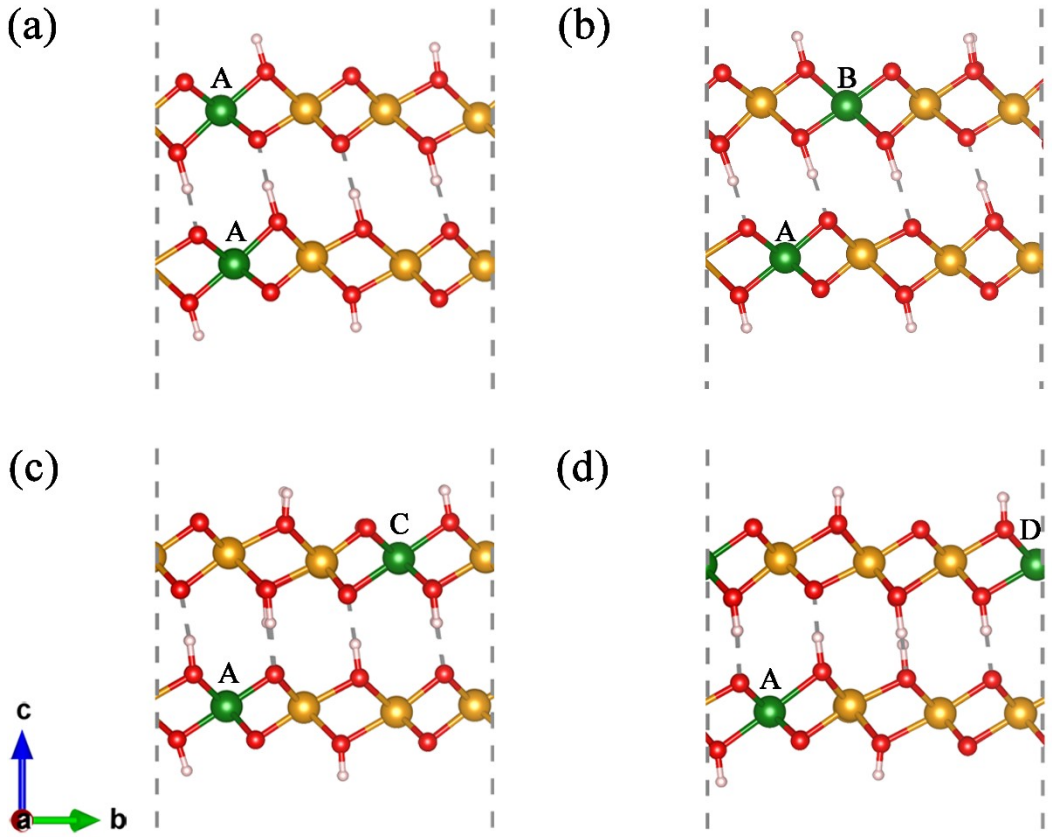

Fig. S6 The geometric structures of (a) $Ni_{25\%}Fe_{75\%}OOH$ (Ni A-A); (b) $Ni_{25\%}Fe_{75\%}OOH$ (Ni A-B); (c) $Ni_{25\%}Fe_{75\%}OOH$ (Ni A-C); (d) $Ni_{25\%}Fe_{75\%}OOH$ (Ni A-D). Yellow, green, red, and pink spheres represent Ni, Fe, O, and H atoms, respectively.

calculated using the following equation: To further evaluate the stability of the catalyst under OER conditions, both its electrochemical stability and thermal stability were examined. The electrochemical stability was assessed by calculating the dissolution potential U_{diss}[6,7], which can be expressed as follows:

$$U_{diss} = U_{diss}^{\circ} - E_{form}/Ne \quad \text{(S13)}$$

where U_{diss}° is the standard dissolution potential of the corresponding bulk metal and Ne is the number of electrons transferred during the dissolution process. In general, a positive U_{diss} value indicates that the catalyst is electrochemically stable under operating conditions. In this work, U_{diss}° and Ne are -0.45 and 2, respectively. The formation energy of an Fe vacancy defect can be

$$E_f(V_{Fe}) = E_{NiFeOOH} - E_{NiFeOOH-V_{Fe}} - E_{Fe} \quad \text{(S14)}$$

Where $E_{NiFeOOH-V_{Fe}}$ and $E_{NiFeOOH}$ represent the total energy of the NiFeOOH without Fe vacancies and the total energy of the NiFeOOH, respectively. E_{Fe} is the energy of an Fe atom. The defect formation energy of $Ni_{75\%}Fe_{25\%}OOH$ (Fe A-C) was calculated to be -3.52 eV. Based on the dissolution potential equation, the corresponding dissolution potential was determined to be 1.31 V, which is markedly higher than 0 V.

This result indicates that the catalyst has strong resistance to electrochemical dissolution and thus favorable electrochemical stability under OER conditions.

We investigated the thermal stability of $Ni_{75\%}Fe_{25\%}OOH$ (Fe A-C) through ab-initio molecular dynamics (AIMD) simulations conducted in a canonical ensemble (NVT) using a Nose-Hoover thermostat with a time step of 1 fs. After 6 ps AIMD simulation at 300 K, the $Ni_{75\%}Fe_{25\%}OOH$ (Fe A-C) monolayer maintained its structural integrity, indicating good thermal stability at room temperature.

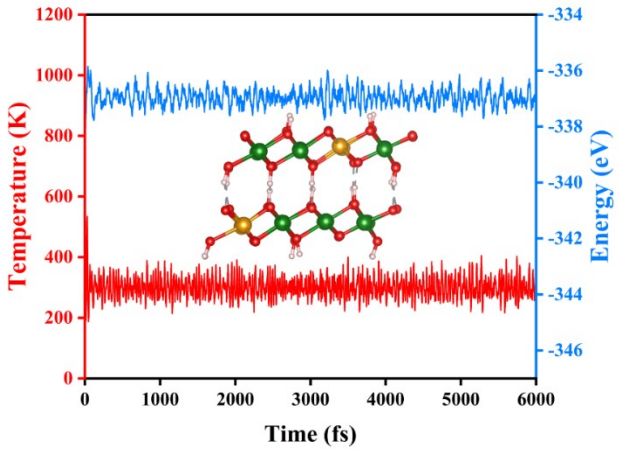

Fig. S7 Energy and temperature variation with AIMD time for $Ni_{75\%}Fe_{25\%}OOH$ (Fe A-C) at 300 K.

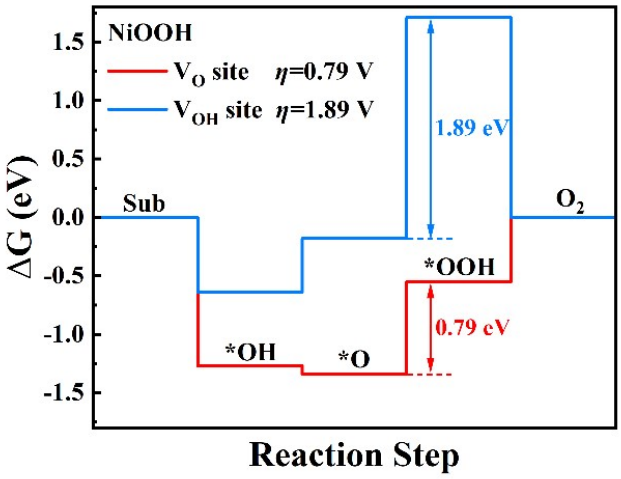

Fig. S8 Gibbs free energy under the standard condition of 1.23 V and overpotential step diagrams of monolayer NiOOH.

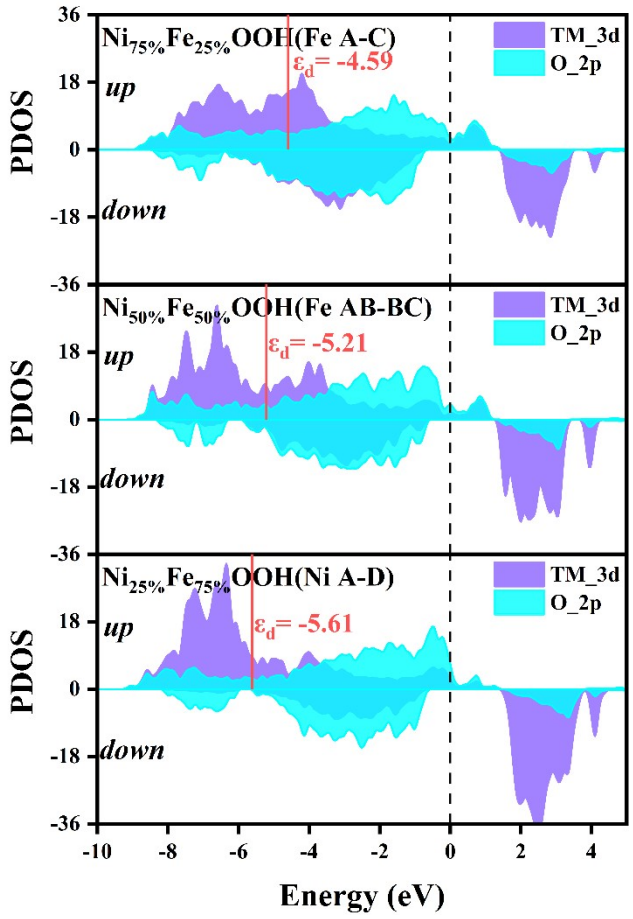

Fig. S9 Projected density of states (PDOS) of the 3d orbitals of the top-layer metal atoms (Ni and Fe) and the 2p orbitals of O in $Ni_{75\%}Fe_{25\%}OOH$ (Fe A-C), $Ni_{50\%}Fe_{50\%}OOH$ (Fe AB-BC), and $Ni_{25\%}Fe_{75\%}OOH$ (Ni A-D). The Fermi level is set at 0 eV.

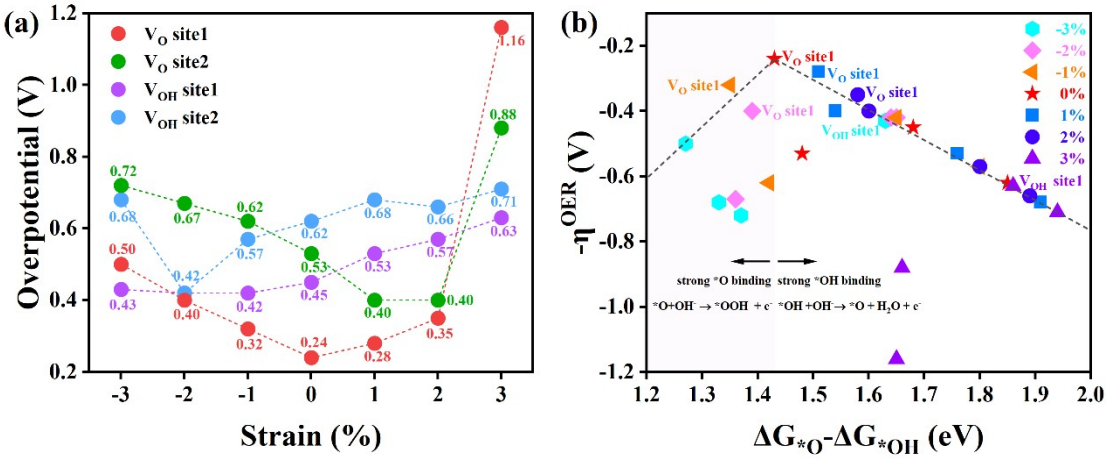

Fig. S10 (a) The OER overpotentials change under biaxial strains ranging from -3% to 3%. (b) 2D volcano plot of OER catalytic activity for $Ni_{75\%}Fe_{25\%}OOH$ (Fe A-C) under biaxial strains.

To investigate whether the strain effect is also applicable to other Fe doping concentrations, we further examined the biaxial strain effect on $Ni_{50\%}Fe_{50\%}OOH$ (Fe AB-BC) at the V_O site2, as shown in Fig. S8. The OER overpotential decreases from

0.42 V to 0.34 V under -2% strain, but the OER overpotential increases to 0.62 V under -3% strain. Under the influence of tensile strain, the overpotential exhibits a steady and incremental increase, attaining values of 0.50 V, 0.55 V, and 0.61 V at strain levels of 1%, 2%, and 3%, respectively. These findings unequivocally confirm that strain engineering remains effective for the $Ni_{50\%}Fe_{50\%}OOH$ (Fe AB-BC) system. Nevertheless, it is evident that the optimal strain range and the degree of activity modulation deviate from those observed in the $Ni_{75\%}Fe_{25\%}OOH$ (Fe A-C) system, thereby highlighting the strain effect's dependence on both doping concentration and the local structural environment.

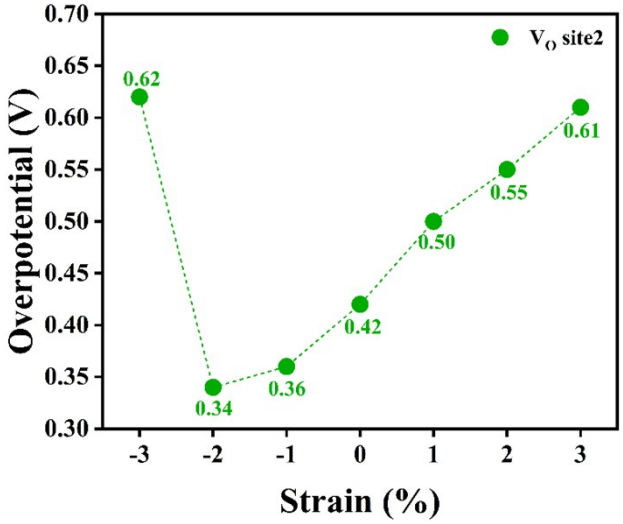

Fig. S11 The OER overpotential of $Ni_{50\%}Fe_{50\%}OOH$ (Fe AB-BC) at the V_O site2 as a function of biaxial strain ranging from -3% to 3%.

To assess the possible role of proton transfer and hydrogen-bond networks in the oxygen evolution reaction (OER) on NiOOH-based catalysts, we further considered a hydrogen-bonded configuration for the most active structure, $Ni_{75\%}Fe_{25\%}OOH$ (Fe A-C). After introducing the hydrogen-bond network[8,9], the calculated overpotential increases from 0.24 V to 0.61 V. This calculation result clearly demonstrates that although the influence of the hydrogen-bond network leads to a certain increase in the overpotential of the OER reaction, this system still exhibits relatively excellent catalytic performance compared with most oxygen-evolution catalysts.

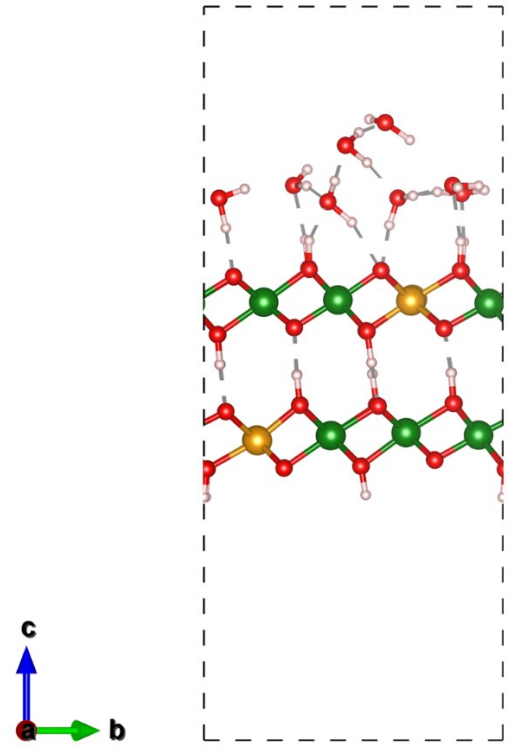

Fig. S12 Schematic structures of $Ni_{75\%}Fe_{25\%}OOH$ (Fe A-C)-$8H_2O$. The green, yellow, red, and pink spheres represent Ni, Fe, O, and H atoms, respectively.

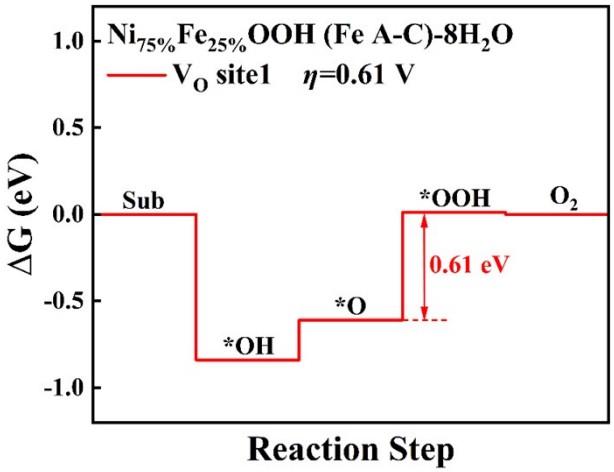

Fig. S13 Gibbs free energy under the standard condition of 1.23 V and overpotential step diagrams of $Ni_{75\%}Fe_{25\%}OOH$ (Fe A-C)-$8H_2O$.

To further clarify the role of Fe doping in OER kinetics, the CI-NEB calculations were performed for the O-O bond formation/evolution process. As shown in Fig. S9, the O-O adsorbed state to the O-O desorbed state pathway already exhibits an overall downhill energy trend. Despite the emergence of a marginal energy increment in proximity to the final configuration of the O-O desorbed state, it is still substantially lower than the initial-state energy. This phenomenon can be ascribed to the attenuated surface interaction within the detached product-like state. These findings unequivocally

indicate that Fe doping not only diminishes the thermodynamic overpotential of the system but also enables oxygen molecules to desorb from the surface without any barrier hindrance.

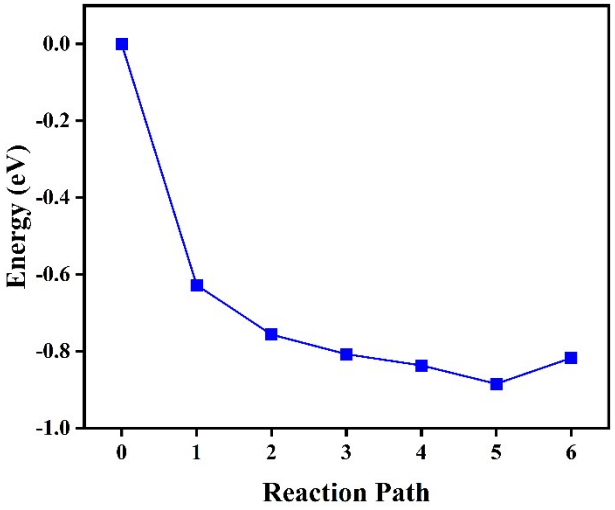

Fig. S14 CI-NEB energy profiles for the O-O bond formation/evolution process in the Fe-doped system.

Table S1. The energies of bilayer NiOOH and $Ni_{75\%}Fe_{25\%}OOH$ (Fe A-C) in ferromagnetic (FM) and antiferromagnetic (AFM) coupling, respectively.

Structure	AFM [eV]	FM [eV]
bilayer NiOOH	-322.50	-322.56
$Ni_{75\%}Fe_{25\%}OOH$ (Fe A-C)	-339.48	-339.52

Table S2. The formation energies per Fe atom (E_f) of the considered $Ni_{25\%}Fe_{75\%}OOH$ structures, $Ni_{50\%}Fe_{50\%}OOH$ structures, and $Ni_{75\%}Fe_{25\%}OOH$ structures.

Structure	Structure	E_f [eV]
$Ni_{75\%}Fe_{25\%}OOH$	Fe A-A	-0.12
	Fe A-B	-0.12
	Fe A-C	**-0.13**
	Fe A-D	-0.10
$Ni_{50\%}Fe_{50\%}OOH$	Fe AB-AB	-0.16
	Fe AB-AC	-0.11
	Fe AB-AD	-0.12
	Fe AB-BC	**-0.19**
	Fe AB-BD	-0.12
	Fe AB-CD	-0.12
	Fe AC-AC	-0.11
	Fe AC-BC	-0.11
	Fe AC-BD	-0.15
	Fe AC-CD	-0.17
$Ni_{25\%}Fe_{75\%}OOH$	Ni A-A	-0.18

	Ni A-B	-0.17
	Ni A-C	-0.06
	Ni A-D	**-0.19**

Table S3. The OER overpotentials at different reaction sites and the vacancy formation energies ($E_f(V_{O/OH})$) for monolayer and bilayer NiOOH.

Structure	site	η (V)	$E_f(V_{O/OH})$ (eV)
Monolayer NiOOH	**V_O site**	**0.79**	**1.03**
	V_{OH} site	1.89	2.22
Bilayer NiOOH	V_O site	0.56	0.98
	V_{OH} site	**0.47**	**2.35**

Table S4. The OER overpotentials at different OER reaction sites and the corresponding vacancy formation energies ($E_f(V_{O/OH})$) for $Ni_{75\%}Fe_{25\%}OOH$ (Fe A-C), $Ni_{50\%}Fe_{50\%}OOH$ (Ni AB-BC), and $Ni_{25\%}Fe_{75\%}OOH$ (Ni A-D).

Structure	Reaction site	η (V)	$E_f(V_{O/OH})$ (eV)
$Ni_{75\%}Fe_{25\%}OOH$ (Fe A-C)	**V_O site1**	**0.24**	**0.55**
	V_O site2	0.53	1.05
	V_{OH} site1	0.45	2.22
	V_{OH} site2	0.62	2.52
$Ni_{50\%}Fe_{50\%}OOH$ (Ni AB-BC)	V_O site1	0.57	1.12
	V_O site2	**0.42**	**0.53**
	V_{OH} site1	0.61	2.51
	V_{OH} site2	0.66	2.74
$Ni_{25\%}Fe_{75\%}OOH$ (Ni A-D)	**V_O site1**	**0.44**	**0.90**
	V_O site2	0.70	1.27
	V_{OH} site1	0.48	2.34
	V_{OH} site2	0.63	2.48

Supplementary References

1 Z. W. Seh, J. Kibsgaard, C. F. Dickens, I. Chorkendorff, J. K. Nørskov and T. F. Jaramillo, *Science*, 2017, **355**, eaad4998.

2 W. Yang, Z. Wang, W. Zhang and S. Guo, *Trends in Chemistry*, 2019, **1**, 259-271.

3 J. K. Nørskov, J. Rossmeisl, A. Logadottir, L. Lindqvist, J. R. Kitchin, T. Bligaard and H. Jónsson, *J. Phys. Chem. B*, 2004, **108**, 17886-17892.

4 Á. Valdés, Z. W. Qu, G.-J. Kroes, J. Rossmeisl and J. K. Nørskov, *J. Phys. Chem. C*, 2008, **112**, 9872-9879.

5 I. C. Man, H. Su, F. Calle-Vallejo, H. A. Hansen, J. I. Martínez, N. G. Inoglu, J. Kitchin, T. F. Jaramillo, J. K. Nørskov and J. Rossmeisl, *ChemCatChem*, 2011, **3**, 1159-1165.

6 X. Guo, J. Gu, S. Lin, S. Zhang, Z. Chen and S. Huang, *J. Am. Chem. Soc.*, 2020, **142**, 5709-5721.

7 X. Wang, H. Niu, X. Wan, A. Wang, F. R. Wang and Y. Guo, *ACS Sustainable Chem. Eng.*, 2022, **10**, 7692-7701.

8 F. Dionigi, Z. Zeng, I. Sinev, T. Merzdorf, S. Deshpande, M. B. Lopez, S. Kunze, I. Zegkinoglou, H. Sarodnik, D. Fan, A. Bergmann, J. Drnec, J. F. D. Araujo, M. Gliech, D. Teschner, J. Zhu, W. X. Li, J. Greeley, B. R. Cuenya and P. Strasser, *Nat Commun*, 2020, **11**, 2522.

9 B. Wen, M. F. Calegari Andrade, L. M. Liu and A. Selloni, *Proc. Natl. Acad. Sci. U.S.A.*, 2023, **120**, e2212250120.